POTENTIAL OF Cs_2TiI_6 PEROVSKITE FILMS AS AN ABSORBER OF SOLAR CELLS

SAMEEN ASLAM

UNIVERSITI SAINS MALAYSIA

2025

POTENTIAL OF Cs_2TiI_6 PEROVSKITE FILMS AS AN ABSORBER OF SOLAR CELLS

by

SAMEEN ASLAM

Thesis submitted in fulfilment of the requirements
for the degree of
Doctor of Philosophy

June 2025

ACKNOWLEDGEMENT

In the name of **Allah**, the Most Gracious, the Most Merciful. I extend all praise and thanks to Allah for His countless blessings and guidance throughout my academic journey and the completion of this thesis.

My deepest gratitude goes to my main supervisor, **Dr. Siti Azrah Mohamad Samsuri**, for her invaluable guidance, constant encouragement, and unwavering support. Her expertise has been instrumental in the successful completion of this research. I also thank my co-supervisor, **Dr. Mohd Zamir bin Pakhuruddin**, for his supportive manner and knowledge.

I am profoundly thankful to my parents and siblings for their unconditional love, patience, and encouragement, which have been my source of strength. Their support has been integral to my achievements.

My heartfelt appreciation goes to my friends, lab fellows and colleagues, who provided constant support and companionship throughout this journey. Special mention to my dear friend **Shawbo** for her unwavering generosity, support, and companionship. Your friendship has been invaluable. I am also sincerely grateful to my wonderful friends **Rozina Kakar**, **Maria Khosa** and **Durdana Khosa**, whose presence and encouragement in foreign country have been a true source of strength.

Special thanks to the NOR lab staff from the School of Physics for their technical assistance, support, and collaboration. Finally, I express gratitude to all who contributed, directly or indirectly, to the successful completion of this thesis. Your support and encouragement are greatly appreciated.

TABLE OF CONTENTS

ACKNOWLEDGEMENT ..... **ii**

TABLE OF CONTENTS ..... **iii**

LIST OF TABLES ..... **viii**

LIST OF FIGURES ..... **x**

LIST OF SYMBOLS ..... **xix**

LIST OF ABBREVIATIONS ..... **xx**

ABSTRAK ..... **xxii**

ABSTRACT ..... **xxiv**

CHAPTER 1 INTRODUCTION **1**

1.1 Introduction 1

1.2 Originality of the Research 6

1.3 Problem Statement 6

1.4 Objectives 9

1.5 Scope of Research 9

1.6 Research Questions 10

1.7 Thesis Outline 10

CHAPTER 2 LITERATURE REVIEW **12**

2.1 Introduction 12

2.2 Perovskites 12

2.3 Structure of Perovskites 16

2.4 Family of perovskites 18

2.4.1 Single halide perovskites 18

2.4.2 Double halide perovskites 19

2.4.3 Vacancy ordered double halide perovskites 23

2.5 Lead-free halide perovskites 25

2.5.1 Single and double halide lead-free halides....26
2.5.2 Vacancy ordered double halide lead-free perovskites....31
2.6 Titanium-based VODHPs....35
2.6.1 Crystal structure of Ti-based VODHPs....35
2.6.2 Synthesis methods for Ti-based VODHPs....36
2.6.3 Optical properties of Ti-based VODHPs....47
2.6.4 Stability of Ti-based VODHPs....49
2.7 Perovskite solar cells....51
2.7.1 Working of Perovskite Solar Cells....55
2.7.2 Solar cell parameters....58
2.8 Device architecture/configuration of perovskite solar cells....60
2.9 Materials for perovskite solar cells....63
2.9.1 Electrode materials for anode and cathode....63
2.9.2 Electron Transport Layers....64
2.9.3 Hole transport layers....65
2.10 Ti-based vacancy ordered double halide perovskites solar cells....66
2.10.1 Experimental studies....66
2.10.2 Computational simulation studies....67
2.11 Challenges in Ti-VODHPs solar cells....77
2.11.1 Large and indirect bandgap nature....77
2.11.2 Low electronic dimensionality....77
2.11.3 Lifetime and stability under high temperature and humidity....78
2.11.4 Difficulties in fabrication of Ti- based VODHP films....78
CHAPTER 3 METHODOLOGY....79
3.1 Introduction....79
3.2 Cs_2TiI_6 VODHP precursor solution preparation....81
3.2.1 Materials used for synthesis of Cs_2TiI_6 VODHPs....81

3.2.2 Experimental procedure for synthesis of Cs_2TiI_6 VODHP precursor solution 83

3.2.3 Synthesis parameters of Cs_2TiI_6 VODHP solution 84

3.3 Preparation of Cs_2TiI_6 VODHP films 86

3.3.1 Cleaning of substrates 87

3.3.2 Variation in deposition techniques 87

3.3.3 Variation in annealing temperature 88

3.3.4 Variation in annealing time 88

3.4 Fabrication of Cs_2TiI_6 VODHP solar cells 89

3.4.1 ITO etching and cleaning 89

3.4.2 ETL preparation 90

3.4.3 Perovskite absorbing layer preparation 92

3.4.4 HTL preparation 92

3.4.5 Metal electrode/back contact deposition 93

3.5 Characterization of Cs_2TiI_6 VODHP films 94

3.5.1 Morphological characterization 95

3.5.2 Structural characterization 97

3.5.3 Optical characterization 99

3.5.4 Electrical characterization 102

3.5.5 Solar simulator 105

CHAPTER 4 RESULTS AND DISCUSSIONS 106

4.1 Introduction 106

4.2 Variation in concentration of precursors of Cs_2TiI_6 VODHP solution 106

4.2.1 Morphological analysis 107

4.2.2 Structural analysis 112

4.2.3 Optical analysis 120

4.3 Variation in the solvent of Cs_2TiI_6 VODHP solution 125

4.3.1 Morphological analysis 126

4.3.2 Structural analysis 130
4.3.3 Optical analysis 133
4.4 Variation in oil bath temperature 135
4.4.1 Morphological analysis 137
4.4.2 Structural analysis 139
4.4.3 Optical analysis 141
4.5 Effect of SnI_4 doping in Cs_2TiI_6 VODHPs 142
4.5.1 Morphological analysis 143
4.5.2 Structural analysis 145
4.5.3 Optical analysis 148
4.6 Variation in deposition techniques of Cs_2TiI_6 VODHP solution 150
4.6.1 Morphological analysis 152
4.6.2 Structural analysis 155
4.6.3 Optical analysis 157
4.7 Variation in annealing temperature of Cs_2TiI_6 VODHP films 159
4.7.1 Morphological analysis 159
4.7.2 Structural analysis 160
4.7.3 Optical analysis 162
4.8 Variation in annealing time of Cs_2TiI_6 VODHP films 164
4.8.1 Morphological analysis 164
4.8.2 Structural analysis 165
4.8.3 Optical analysis 168
4.9 Extended analysis for optimum Cs_2TiI_6 VODHP films 170
4.9.1 Structural analysis 170
4.9.2 Optical analysis 172
4.9.3 Optical stability 174
4.9.4 Hall effect 179

4.9.5 I-V analysis 182
4.10 Fabrication of Cs_2TiI_6 Perovskite Solar Cells 185
4.10.1 ETL characterization 185
(a) Morphological analysis 185
(b) Optical analysis 186
4.10.2 Solar cell performance of Cs_2TiI_6 device 188
CHAPTER 5 CONCLUSION AND FUTURE RECOMMENDATIONS 192
5.1 Conclusion 192
5.2 Future Work 194
REFERENCES 195
LIST OF PUBLICATIONS

LIST OF TABLES

Page

Table 1.1 Ti-based VODHPs with different synthesis methods and reported bandgaps.....5

Table 2.1 Summary of various HDPs synthesized by various techniques.....22

Table 2.2 Ionic radius and electronic structure of various metal cations.....25

Table 2.3 Various Pb-free perovskites and their corresponding device architecture and parameters.....30

Table 2.4 Pb-free VODHPs and their bandgaps and solar device parameters. 35

Table 2.5 Band gap of Ti-based VODHPs with different synthesis methods....48

Table 2.6 History of perovskite solar cells with their device configuration and efficiencies from 3.81% to 25.7 % [48]. 54

Table 2.7 Comparison of performance with different device configurations. ...67

Table 2.8 Summary of the optimum thickness of Ti-based VODHP films for different device configurations.....69

Table 2.9 Summary of the best performance of Ti-based VODHPs solar cells with their respective ETLs. 71

Table 2.10 Summary of the best performance of Ti-based VODHPs solar cells with their respective HTL material. 74

Table 2.11 Performance comparison of different back contact materials in Cs_2TiBr_6 PSCs [185].....76

Table 2.12 Performance comparison of different back contact materials in Cs_2TiI_6 PSCs [41].....76

Table 3.1 List of chemicals. 81

Table 3.2 Parameters for sputtering TiO_2 as ETL.....92

Table 3.3 Parameters for spin-coating HTL (Spiro-Ometad).....93

Table 4.1 Elemental composition of Cs_2TiI_6 VODHP films with varying concentrations. 111

Table 4.2 The chemical composition and XRD data of Cs_2TiI_6 VODHP. 115

Table 4.3 XRD peak positions with corresponding Miller indices for Cs_2TiI_6 VODHPs. 117

Table 4.4 Structural parameters and bond lengths calculated for Cs_2TiI_6 VODHPs. 119

Table 4.5 Direct and indirect optical bandgaps of Cs_2TiI_6 VODHP films with a variation of precursor concentration..... 123

Table 4.6 The structural parameters from XRD data in different solvents. 132

Table 4.7 The structural parameters from XRD data with dopant concentration. 147

Table 4.8 The variation of structural parameters with varying annealing temperatures. 161

Table 4.9 The variation in structural parameters with variation of annealing time..... 167

Table 4.10 Optimal parameters for Cs_2TiI_6 VODHPs. 170

Table 4.11 The electrical properties of Cs_2TiI_6 VODHP films. 182

Table 4.12 Average solar cell parameters for Cs_2TI_6 VODHP and $MAPBI_3$ perovskite solar cell devices..... 191

LIST OF FIGURES

Page

Figure 2.1 (a) Perovskite emission wavelength tuning by halide composition, (b) Photoluminescence spectra of $CsPbX_3$ perovskites with varying halide ratios, (c) Absorption and PL spectra of $CsPbX_3$ perovskites showing bandgap tunability [64][65]. 14

Figure 2.2 Crystal structure of ABX_3 perovskite and commonly used elements at A, B, and X sites, along with their ionic radii (in Å) [80]..... 16

Figure 2.3 Overview of halide perovskites (a) Standard ABX_3 cubic halide perovskites, (b) Common orthorhombic and tetragonal disordered perovskites arise from the octahedra tilting [87] and (c) 3D, 2D, 1D, and 0D crystal structures of ABX_3 perovskites..... 17

Figure 2.4 (a) and (b) Schematic view of B^+/B^{3+} cation substitution from Pb halide perovskites ($APbX_3$) to double perovskites ($A_2B^+B^{3+}X_6$) [100], (c) Selection of cations and anions for $A_2B^+B^{3+}X_6$ perovskites..... 20

Figure 2.5 (a) XRD pattern and (b) SEM image of the prepared $Cs_2AgBiBr_6$ double perovskite thin films [111] (c) Typical absorption spectrum of $Cs_2AgBiBr_6$ films with the inset showing the absorption onset at 610 nm [110] (d) Absorbance spectrum of $Cs_2AgBiBr_6$ powder (Inset: Tauc plot showing the characteristics of an indirect bandgap) [103] (e) Steady-state room-temperature PL spectrum of a powdered $Cs_2AgBiBr_6$ sample upon 500 nm excitation. (Inset: low-temperature PL spectrum) [103] (f) Time-resolved room-temperature PL and fits for the PL decay time (τ) in powder and single-crystal samples) [103]. 21

Figure 2.6 Schematic of the relationship between ABX_3 perovskite and A_2BX_6 (vacancy-ordered) double perovskite [17]. 23

Figure 2.7 (a) Perovskite crystal structure of $CH_3NH_3SnI_3$ [138], (b) Bandgap energies of different combinations in an $ABSn_3$ perovskite structure [133]. 26

Figure 2.8 Absorption and PL spectra of the various lead free ABX_3 perovskites [139][143]. 27

Figure 2.9 (a) Direct and indirect bandgap values of various Ge-based perovskite materials compared with $MAPbI_3$, (b) UV-Vis absorption spectra of $CsSnI_3$, $CsGeI_3$, $MAGeI_3$, and $FAGeI_3$, (c) J-V curves for $CsGeI_3$ and $MAGeI_3$, highlighting differences in photovoltaic performance. SEM images of $CsGeI_3$ (d), $MAGeI_3$ (e), and $FAGeI_3$ [150]. 28

Figure 2.10 (a) Scanning Electron Microscopy (SEM) images of a Cs_2SnI_6 film [25] (b) XRD patterns of Cs_2SnI_6 thin film and powder obtained via oil-bath method. The inset shows the solution obtained upon dissolving the powder in DMF (c) The absorption and photoluminescence (PL) UV spectra of the Cs_2SnI_6 film indicate its direct bandgap of about 1.48 eV [24] (d) Calculated absorption coefficients for A_2BX6 (A = Rb, Cs; B = Sn, Pd, Pt; X = Cl, Br, I) compounds [18] (e) UV–vis spectra of Cs_2PdBr_6 (f) PL spectra of Cs_2PdBr_6 (excited at 500 nm) [121]..... 32

Figure 2.11 Crystal structure of Ti-based VODHPs (A_2TiX_6) [173]. 36

Figure 2.12 (a) and (b) Schematic illustration of the vapor-based synthesis of Cs_2TiBr_6 perovskite thin film, (c) UV-vis spectra of Cs_2TiBr_6 HP thin film (inset: photograph of the final Cs_2TiBr_6 thin film), and (d) Tauc plot and PL spectrum of the Cs_2TiBr_6 HP thin film [33]. 38

Figure 2.13 (a) Schematic illustration of melt-crystallization method in quartz tube, (b) Experimentally measured absorption spectra of Cs_2TiI_6, $Cs_2TiI_4Br_2$, $Cs_2TiI_2Br_4$, and Cs_2TiBr_6 HPs [32]. 39

Figure 2.14 (a) Synthesized Cs_2TiCl_6, Cs_2TiBr_6, and $Cs_2TiBr_2Cl_4$ perovskites using solution-based method, (b) absorption spectra of Cs_2TiCl_6, Cs_2TiBr_6, and $Cs_2TiBr_2Cl_4$ films. Tauc plots of absorption

coefficients versus photon energy, (c) for indirect allowed transitions, and (d) for direct allowed transitions [36]. 41

Figure 2.15 (a) Schematic representation of Cs_2TiBr_6 nanocrystal synthesis: injection of TMS-Br into precursor solution at high temperature (inset: thin films of Cs_2TiBr_6 and Cs_2TiI_6 [44], (b) Absorption spectra of $Cs_2TiBr_{6-x}I_x$ NCs [43]. 43

Figure 2.16 (a) Schematic representation of ball milling process, (b) X-ray diffraction patterns of cesium-titanium halides, and (c) the direct and indirect bandgaps of Cs_2TiBr_6 obtained from Kubelka-Munk plot from reflectance spectra [42]. 45

Figure 2.17 (a) Schematic diagram of the MW-mediated synthesis of a Cs_2TiBr_6 powder, (b) X-ray photoelectron spectrum (XPS) with labeled peaks, (c) absorption and PL emission spectra, and (d) Tauc plot from the absorption spectrum of the MW-synthesized Cs_2TiBr_6 powders [47]. 46

Figure 2.18 (a) UV-Vis absorbance spectra of Cs_2TiBr_6 powder measured on day 1 and after 8 weeks, showing changes in optical properties over time, (b) XRD patterns of Cs_2TiBr_6 powder on day 1 and after 8 weeks, indicating the formation of CsBr impurity peaks (marked with *), (c) Structural degradation of Cs_2TiBr_6 powder over a certain time, (d) Phase shifting of Cs_2TiBr_6 peaks to CsBr peaks, (e) XRD patterns of Cs_2TiCl_6 powder at different time intervals, showing the emergence of CsCl impurity peaks (marked with *)[201]..... 51

Figure 2.19 The progress of solar cell types and power conversion efficiencies of laboratory fabricated PV devices from 1975 to 2024 as certified by the National Renewable Energy Laboratory (NREL) [48]. 52

Figure 2.20 (a) Schematic illustration of a solar cell, and (b) Schematic of the mechanism of working PSCs under illumination [220]. 56

Figure 2.21 Solar cell parameters are highlighted in a typical J-V characteristic curve for a perovskite-based device [222]. 58

Figure 2.22 Schematic illustration of PSC device architectures.....61

Figure 2.23 Variety of architectures for perovskite solar cells [227].....62

Figure 2.24 Energy levels of different layers used in PSCs [220].....65

Figure 2.25 (a) Energy band alignment of FTO/TiO_2/C60/ Cs_2TiBr_6/P3HT/Au device, (b) J-V curves of Cs_2TiBr_6 with and without the presence of the C60 interfacial layer, and (c) Stabilized PCE output at the maximum power points of the PSCs with and without the presence of the C60 interfacial layer [33].....67

Figure 2.26 Summary of the energy level of ETL, Ti-based VODHP, Cs_2TiBr_6, and HTL [256][250][28][33].....75

Figure 3.1 Flow chart of experimental steps. 80

Figure 3.2 Schematic diagram for the preparation of Cs_2TiI_6 VODHPs. 84

Figure 3.3 Schematic representation of fabrication of solar cell device.....89

Figure 3.4 (a) Schematic diagram of radiofrequency (DC/RF) magnetron sputtering system [267], and (b) The image of direct current and radiofrequency (DC/RF) magnetron sputtering system (Edwards Auto 500 model) used in NOR lab USM. 91

Figure 3.5 (a) Schematic diagram of working principle of thermal evaporator [268], (b) Image of thermal evaporation system (Edwards Auto 306 model). 94

Figure 3.6 (a) Schematic diagram working principle of field emission scanning electron microscopy (FESEM) [269], and (b) Image of field emission scanning electron microscopy (FESEM) (model: FEI Nova NanoSEM 450) in NOR lab. 96

Figure 3.7 (a) Schematic diagram of components of X-ray diffractometer [270], and (b) Image of XRD (Model PANalytical X'Pert PRO MRD PW3040). 98

Figure 3.8 (a) Schematic image of the working of Raman spectroscopy [271], and (b) Raman from MIMOS Malaysia.....99

Figure 3.9 (a) Schematic image of working of UV-Vis-NIR spectroscopy [272], (b) UV-Visible Spectrophotometer Model Cary 5000 UV-VIS-NIR. 100

Figure 3.10 (a) Schematic image of the working principle of PL [273], (b) TRPL system in Research School of Physics Australian National University. 102

Figure 3.11 Image of Hall effect HL5500PC system with perovskite sample having electrode. 103

Figure 3.12 CV/IV system Model 82 Simultaneous in NOR-lab. 104

Figure 3.13 (a) Schematic diagram of LED-based light source solar simulator [274], and (b) Photograph image (model: TMS-2X2 Forter Technology). 105

Figure 4.1 Top surface FESEM images and corresponding EDS spectra of Cs_2TiI_6 films with varying concentrations of TiI_4 as (a) 0.20 mmol, (b) 0.25 mmol, (c) 0.30 mmol, (d) 0.35 mmol, (e) 0.40 mmol and (f) 0.50 mmol. 109

Figure 4.2 (a) Top surface FESEM image of 0.30 mmol Cs_2TiI_6 VODHP film, (b) top surface image of Cs_2TiI_6 VODHP film with measured grain size, and (c) EDX spectra of Cs_2TiI_6 VODHP film with elemental mapping of each element. 112

Figure 4.3 XRD patterns of Cs_2TiI_6 VODHP films with the variation of molar concentration. 113

Figure 4.4 XRD patterns of Cs_2TiI_6 VODHP film with the corresponding simulated patterns 116

Figure 4.5 Crystal structure of (a) ideal perovskite: $A(B^{2+})X_3$ ((221)), (b) Vacancy-ordered double *Fm*3*m* perovskite $A_2(B^{4+})X_6$ ((225)), (c) Primitive unit cell of the of Cs_2TiI_6 with corresponding Wyckoff positions, and (d) Bonding lengths between atoms produced using VESTA software. 118

Figure 4.6 (a) UV absorbance of Cs_2TiI_6 VODHP film with variation of precursor concentration, (b) direct and indirect bandgap of 0.30

mmol Cs_2TiI_6 VODHP film, (c) direct and (d) indirect optical bandgap of Cs_2TiI_6 VODHP films with variation of precursor concentration. 123

Figure 4.7 PL intensity of Cs_2TiI_6 perovskite film with variable concentration of TiI_4. 124

Figure 4.8 Top surface FESEM images of Cs_2TiI_6 VODHP films with varying solvents at 500x (Left) and 1000x (Right) (a) DMSO, (b) DMF, and (c) DMSO: DMF. 128

Figure 4.9 As synthesized Cs_2TiI_6 VODHP films with various solvents. 129

Figure 4.10 EDS Spectra for various solvents (a) DMSO, (b) DMF and (c) DMSO: DMF (Inset: elemental composition for the corresponding image) 130

Figure 4.11 XRD patterns of Cs_2TiI_6 VODHP films with the variation of solvents 131

Figure 4.12 (a) UV absorbance of Cs_2TiI_6 VODHP films with variation of solvents (b) direct bandgap of Cs_2TiI_6 VODHP films for various solvents (c) indirect bandgap of Cs_2TiI_6 VODHP films for various solvents 133

Figure 4.13 PL absorption peaks of Cs_2TiI_6 VODHP films with variation of solvents 134

Figure 4.14 (a) The formation of Cs_2TiI_6 VODHP solution at 90 ^oC, and (b) The initial formation of crystals in Cs_2TiI_6 VODHP solution at 120 ^oC. 136

Figure 4.15 Top surface FESEM images of Cs_2TiI_6 film with variation of temperature of Oil bath (a), (b) 60 ^oC and (c), (d) 90 ^oC. 137

Figure 4.16 EDS Spectra for Cs_2TiI_6 films with variation of temperature of oil bath (a) and (b) 60 ^oC, and (c) and (d) 90 ^oC. Inset: elemental composition for corresponding elements. 139

Figure 4.17 XRD pattern for Cs_2TiI_6 VODHP films prepared from variation in oil bath temperature at 60 ^oC and 90 ^oC. 140

Figure 4.18 UV-Vis absorbance for films prepared from variation in oil bath temperature at 60°C and 90°C. 141

Figure 4.19 Top surface FESEM images and EDS spectrum of Cs_2TiI_6 VODHP films doped with varying concentrations of SnI_4. 144

Figure 4.20 XRD pattern for doped and undoped Cs_2TiI_6 VODHP films with various concentrations of dopant SnI_4 146

Figure 4.21 (a) UV-Vis absorbance for doped and undoped Cs_2TiI_6 VODHP films with various concentrations, (b) Graph of increasing bandgap with increasing concentration, (c) The direct band gap of doped and undoped Cs_2TiI_6 VODHP films with various concentrations, and (d) Indirect band gap for doped and undoped Cs_2TiI_6 VODHP films with various concentrations. 149

Figure 4.22 The Cs_2TiI_6 VODHP film with their thickness, (a) drop-cast film, (b) spin-coated film, and (c) immersed film, as synthesized and after 15 minutes. 151

Figure 4.23 Top surface FESEM images of Cs_2TiI_6 films at 500x (left) and 1000x (right) (a) Drop-casted film, (b) Immersed film, and (c) Spin-coated film. 153

Figure 4.24 EDS Spectra of Cs_2TiI_6 VODHP (a) Drop-casted film, (b) Immersed film, and (c) Spin-coated film. 155

Figure 4.25 XRD patterns of Cs_2TiI_6 VODHP (a) Drop-casted film, (b) Immersed film, and (c) Spin-coated film. 156

Figure 4.26 (a) Absorbance Spectra of drop-casted, immersed, and spin-coated Cs_2TiI_6 VODHP films, (b) Direct and indirect bandgap of drop-casted Cs_2TiI_6 VODHP films, and (c) Indirect bandgap of spin-coated and immersed Cs_2TiI_6 VODHP films. 158

Figure 4.27 Top surface FESEM images of Cs_2TiI_6 VODHP films at various annealing temperatures 160

Figure 4.28 (a) XRD pattern for Cs_2TiI_6 VODHP films at various annealing temperatures, and (b) various annealed Cs_2TiI_6 VODHP films. 161

Figure 4.29 UV-Vis absorbance for Cs_2TiI_6 VODHP films at various annealing temperatures. 163

Figure 4.30 Top surface FESEM images of Cs_2TiI_6 VODHP films at various annealing times 165

Figure 4.31 (a) XRD pattern for Cs_2TiI_6 VODHP films at various annealing times, and (b) various annealed Cs_2TiI_6 VODHP films at different times. 166

Figure 4.32 UV-Vis absorbance for Cs_2TiI_6 VODHP films at various annealing times. 168

Figure 4.33 Raman shifts for Cs_2TiI_6 VODHP films. 171

Figure 4.34 TRPL decay curves of Cs_2TiI_6 VODHP film. 173

Figure 4.35 (a) Absorbance of perovskite film over time, and (b) degradation/aging of Cs_2TiI_6 VODHP films from day 1 to day 12. 175

Figure 4.36 (a) Refractive index *n* and extinction coefficient *k* values of Cs_2TiI_6 VODHP film, and (b) optical conductivity σ of Cs_2TiI_6 VODHP film. 177

Figure 4.37 (a) Real and imaginary part of the dielectric constant of Cs_2TiI_6 VODHP film, and (b) tan δ for the Cs_2TiI_6 VODHP films. 178

Figure 4.38 Cs_2TI_6 VODHP films for (a) Hall effect and (b) IV characteristics. 181

Figure 4.39 I-V characteristics of (a) Cs_2TiI_6 perovskite on glass, (b) Cs_2TiI_6 perovskite on glass-TiO_2, (c) Cs_2TiI_6 perovskite ITO and (d) Cs_2TiI_6 perovskite on ITO-TiO_2 184

Figure 4.40 (a) Top surface image of sputtered TiO_2 on glass (Inset: thickness of TiO_2 film), and (b) AFM image of TiO_2 on glass. 186

Figure 4.41 TiO_2 (a) Transmittance spectra and (b) Absorbance spectra (Inset: bandgap of TiO_2) 187

Figure 4.42 (a) Cross-section of Cs_2TiI_6 VODHP device, and (b) Schematic diagram of Cs_2TiI_6 VODHP device. 188

Figure 4.43 JV curves of (a) Cs_2TiI_6 VODHP solar cell device, and (b) $MAPbI_3$ perovskite solar cell device. 189

Figure 4.44 Average V_{OC}, J_{SC}, FF, and PCE of Cs_2TiI_6 VODHP solar cell devices 190

LIST OF SYMBOLS

α	Absorption coefficient
Ag	Silver
Al	Aluminum
Au	Gold
β	Full Width at half-maximum
CsI	Cesium Iodide
^oC	Degree Celcius
δ	Dislocation density
D	Crystallite size
d	Diffusion constant
E_g	Band gap
ε	Microstrain
ε_o	Dielectric constant
h	Planks constant
k	Extinction coefficient
L	Diffusion length
λ	Wavelength
μ	Octahedral factor
n	Refractive index
σ	Optical conductivity
TiI_4	Titanium Tetra-Iodide
t	Tolerance factor
θ	Diffraction angle
υ	Frequency

LIST OF ABBREVIATIONS

AFM	Atomic force microscopy
CIGS	Copper Indium Gallium Selenide
CuSCN	Copper (I) Thiocyanate
DMSO	Dimethyl Sulfoxide
DMF	Dimethyl Formamide
DSSC	Dye Sensitized solar cells
EDS/EDX	Energy Dispersive X-ray Spectroscopy
ETL	Electron transport Layer
FESEM	Field Emission Scanning Electron Microscopy
FF	Fill Factor
FTO	Fluorine Tin oxide
HCl	Hydrochloric acid
HDPs	Halide Double perovskites
HTM/ HTL	Hole transport material/ Hole Transport Layer
HOMO	Highest occupied molecular orbital
IPA	Isopropyl Alcohol
ITO	Indium Tin oxide
IV	Current Voltage
J_{SC}	Short-circuit Current
LEDs	Light Emitting diodes
Li-TFSI	Lithium bis (triflouromethylsulfonyl)imide
LUMO	Lowest occupied molecular orbital
MSM	Metal Semiconductor Metal

PAW	Projector Augmented-Wave
PEAI	Phenethyl ammonium iodide
PL	Photoluminescence
PSCs	Perovskite Solar Cells
PV	Photo Voltaic
PCE	Power Conversion Efficiency
QDSSCs	Quantum Dot Solar Cells
RMS	Root mean square
RF	Radio frequency
SCAPS	Solar Cell Capacitance Simulator
TCO	Transparent Conductive Oxide
TRPL	Time Resolved Photoluminescence
UV	Ultraviolet
VASP	Vienna Ab initio Simulation Package
V_{OC}	Open-circuit Voltage
VODHP	Vacancy Order Double Halide Perovskites
XRD	X-ray Diffraction

POTENSI FILEM PEROVSKIT Cs_2TiI_6 SEBAGAI PENYERAP SEL SURIA

ABSTRAK

Kemajuan pesat bahan berasaskan perovskit dalam fotovoltaik telah menarik minat yang meluas kerana sifat optoelektroniknya yang luar biasa dan potensinya untuk penukaran tenaga suria yang berkos efektif. Namun, kebimbangan terhadap ketoksikan, kesan terhadap alam sekitar, dan sekatan peraturan berkaitan dengan plumbum (Pb) dalam perovskit halida konvensional telah mendorong penerokaan struktur alternatif. Perovskit dwi-halide bertertib kekosongan (VODHP) telah muncul sebagai calon yang menjanjikan dalam fotovoltaik, dengan tujuan untuk mengatasi kekangan yang dikaitkan dengan bahan berasaskan plumbum. Bahan-bahan ini menawarkan kelebihan tambahan seperti jurang jalur tenaga yang boleh dimanipulasi dan sifat optoelektronik yang luar biasa, seperti penyerapan optik yang tinggi, mobiliti yang tinggi, panjang resapan yang panjang, dan sifat pengangkutan cas yang unggul, menjadikannya calon yang serba boleh untuk pelbagai aplikasi. Tesis ini memberi tumpuan kepada sintesis dan pencirian VODHP berasaskan titanium, Cs_2TiI_6. Penggunaan kaedah sintesis berasaskan larutan menawarkan pendekatan baharu untuk menghasilkan bahan-bahan ini. Pelbagai parameter, seperti variasi kepekatan prekursor, jenis pelarut, suhu sintesis, dan kesan doping SnI_4 dalam Cs_2Ti_6 VODHP turut dipertimbangkan bagi memperoleh larutan Cs_2Ti_6 VODHP yang optimum. Kajian ini bukan sahaja tertumpu kepada sintesis, tetapi turut meneroka dengan mendalam ciri-ciri struktur, optik, dan elektrik filem Cs_2Ti_6 VODHP, bagi menonjolkan potensinya dalam aplikasi praktikal. Komposisi filem Cs_2Ti_6 VODHP disahkan melalui Spektroskopi Serakan Tenaga Elektron (EDS) dengan nisbah yang dikehendaki iaitu 2:1:6. Corak Pembelauan Sinar-X (XRD) menunjukkan struktur

kubik bagi Cs_2Ti_6 VODHP dengan parameter kisi berukuran 11.61 Å. Analisis optik menggunakan spektroskopi UV-Vis menunjukkan penyerapan optik yang kuat dengan jalur tenaga terus dan tidak terus dalam julat 1.47–1.65 eV. Pengukuran kesan Hall menunjukkan konduksi jenis-N dengan kepekatan pembawa sebanyak 10^{14} cm^{-3} dan mobiliti sekitar ~70 cm^2/Vs. Filem Cs_2TiI_6 VODHP menunjukkan tingkah laku fotokonduktif apabila didedahkan kepada cahaya. Tambahan pula, satu peranti Cs_2TiI_6 VODHP telah difabrikasi dengan seni bina peranti ITO/TiO_2/Cs_2Ti_6/Spiro-OMeTAD/Au, dan mencapai V_{OC} sebanyak ±0.84 V, J_{SC} sebanyak ±0.05 mA/cm^2, FF = ±0.58 dan kecekapan penukaran kuasa (PCE) sebanyak ±0.05%. Perbandingan dengan $MAPbI_3$ menunjukkan bahawa Cs_2Ti_6 VODHP berpotensi untuk digunakan sebagai lapisan penyerap dalam peranti sel suria. Dengan penambahbaikan berterusan, Cs_2Ti_6 VODHP berkemungkinan menjadi alternatif yang berdaya maju dalam pembangunan sel suria bebas plumbum. Kajian ini menawarkan kaedah larutan yang ringkas untuk mensintesis Cs_2Ti_6 VODHP berasaskan titanium, sekali gus menyerlahkan potensinya sebagai bahan mesra alam untuk sel suria generasi akan datang.

POTENTIAL OF Cs_2TiI_6 PEROVSKITE FILMS AS AN ABSORBER OF SOLAR CELLS

ABSTRACT

The rapid advancement of perovskite-based materials in photovoltaics has garnered substantial interest due to their exceptional optoelectronic properties and potential for cost-effective solar energy conversion. However, concerns over the toxicity, environmental impact, and regulatory restrictions of lead (Pb) in conventional halide perovskites have prompted the exploration of alternative structures. Vacancy-ordered double halide perovskites (VODHPs) have emerged as promising candidates in photovoltaics, aiming to overcome the limitations associated with lead-based materials. These materials offer the added advantages of tunable bandgaps and exceptional optoelectronic properties, such as high optical absorption, high mobility, long diffusion lengths, and superior charge-transport properties, making them versatile candidates for various applications. This thesis focuses on the synthesis and characterization of titanium-based VODHPs, Cs_2TiI_6. The adoption of a solution-based synthesis method offers a novel route for fabricating these materials. Various parameters, such as variations in the precursor's concentration, solvents, synthesis temperature, and the effect of doping SnI_4 in Cs_2TiI_6 VODHPs, are considered to achieve the optimal Cs_2TiI_6 VODHP solution. The investigation extends beyond synthesis to comprehensively explore the structural, optical, and electrical properties of Cs_2TiI_6 VODHP films, highlighting their potential for practical applications. The composition of Cs_2TiI_6 VODHP film is confirmed by Electron Dispersive Spectroscopy (EDS) as the desired ratio of 2:1:6. X-ray Diffraction (XRD) reveals a cubic structure for Cs_2TiI_6 VODHP with lattice parameter of 11.61 Å. Optical analysis

using UV-Vis spectroscopy demonstrates strong optical absorption with direct and indirect bandgap in the range of 1.47-1.65 eV. Hall effect measurements indicate *N*-type conduction with a carrier concentration of 10^{14} cm^{-3} and mobility of ~70 cm^2/Vs. Cs_2TiI_6 VODHP films exhibit photoconductive behaviour under illumination. Furthermore, a Cs_2TiI_6 VODHP, with a device architecture of ITO/TiO_2/Cs_2TiI_6/Spiro-OMeTAD/Au, is fabricated, achieving a V_{OC} of ±0.84 V, J_{SC} of ±0.05 mA/cm^2, *FF* = ±0.58 and power conversion efficiency (PCE) of ±0.05%. When comparing these results with $MAPbI_3$, it becomes evident that Cs_2TiI_6 VODHPs have potential to be used as absorber layers in solar cell devices. With continued refinement, Cs_2TiI_6 VODHPs could become a viable alternative in the development of lead-free solar cells. This study offers a simple solution method for synthesizing titanium based Cs_2TiI_6 VODHPs, highlighting their potential as eco-friendly materials for the next-generation solar cells.

CHAPTER 1

INTRODUCTION

1.1 Introduction

The rising global energy demand calls for extensive research into renewable sources, with solar energy standing out for its potential to convert a substantial amount of solar radiation into electricity. Among the various solar cell technologies used in commercial applications, materials like GaAs and CdTe face limitations in efficiency due to intrinsic material constraints, along with challenges such as limited light absorption, rigidity, and high production costs. To tackle these issues, a considerable focus has shifted to the usage of perovskite semiconductor material.

Over the past decade, perovskite-based materials have garnered immense interest in its potential application in photovoltaics. Perovskites are crystals of chemical compounds serving as semiconductors in solar devices. Perovskite-structured material was first used in solar cells as an alternative to replace conventional dye in liquid dye-sensitized solar cells (DSSC) [1]. The compatibility of perovskite materials as solar cell light harvesters related to its exceptional optoelectronic properties, with high absorption coefficient, tuneable band gap, low excitation binding energy, long charge carrier diffusion length and excellent electron and hole transport properties has contributed to its remarkable performance[2][3]. Perovskites are organic-inorganic compounds with the chemical formula of ABX_3, where A is a single cation (Cs^{+1} or Rb^{+1}) or organic ammonium cation (MA or FA) located at the centre of unit cell; B is a divalent metal cation located at corners, and X is a single halide anion located at the edges of the unit cell.

Currently, the highest power conversion efficiency (PCE) of single-junction perovskite solar cells (PSCs) has reached an experimental value of 26.7% [4], exceeding

the record efficiency of copper indium gallium selenium (CIGS) solar cells (~23.6 %) and approaching that of crystalline-Si solar cells (~27.6%). $MAPbI_3$ with chemical formula ($CH_3NH_3PbI_3$) is the most studied perovskite photovoltaic, identifying as champion absorber material in PSCs having an absorption coefficient $\alpha = 5 \times 10^4$ cm^{-1} in the red [5], long diffusion length (~ 1μm) and band gap ~1.6 eV [6]. Before these perovskites were widely implemented and industrialized, several drawbacks related to perovskite-based photovoltaics needed to be addressed. The primary concerns associated with Pb-based perovskites are poor stability and high toxicity. The organic cations ($MAPbI_3$ and $FAPbI_3$) can quickly degrade into harmful compounds upon exposure to external stimuli like moisture, UV irradiation, increased temperature and oxygen [7][8][9]. These Pb-based perovskites release PbI_2 on degradation, which is toxic [10][11]. As a result of increased oxidation, when Pb is exposed to the human body, it affects multiple body systems and organs (nervous, reproductive, and kidney), particularly young children [12]. Addressing the toxicity and stability issues of Pb-based HPs is a significant challenge. To overcome this, researchers have explored substituting Pb^{2+} in conventional perovskites, with alternative metal elements that have comparable ionic radii (1.19 Å) [13]. Among these, Tin (Sn) and Germanium (Ge) from group 14, as well as the trivalent Bi^{3+} and Sb^{3+} from group 15, have emerged as promising candidates due to their similar electronic configurations [14][15] [16]. While some efforts in this area have been successful, ongoing research continues to explore these and other potential substitutes.

One of the alternate structures designed to replace Pb with other tetravalent cations is vacancy-ordered double halide perovskites (VODHPs) having a general formula of A_2BX_6 (where A = organic/inorganic cations, B = metal cations and X= halide anions) [17][18][19]. The unit cell of ABX_3 is doubled along all three

crystallographic axes, and every other B-site cation is removed to create a distinct structure from the typical perovskite, known as a VODHP. The most studied VODHP as a solar cell absorber is Cs_2SnX_6 (X = Cl, Br, I), due to its strong optical absorption tunable bandgap, low effective mass, and high defect tolerance, making it a promising candidate for efficient, eco-friendly, and versatile solar energy conversion applications. [20][21][22][23]. The experimental band gap of Cs_2SnI_6 has been reported to be in the region of 1.3–1.6 eV [23], and the PCE recorded extremely low, around 1% [24] due to insufficient stability, as it decomposes in the air, leaving behind CsI as an impurity [25]. Moreover, moderate electron mobility [26], high resistivity [27], and a high defect density at the interface [28] also contributed to the low PCE. Due to that, other non-toxic transition metals with a +4 oxidation state, such as Palladium [29], Tellurium [30], Zirconium [31], and Titanium [32][33] have been explored to replace Sn^{+4} in Cs_2SnX_6 (X = Cl, Br, I) VODHPs.

The titanium (Ti)-based VODHPs, Cs_2TiX_6 (X = Cl, Br, I) stand out as a potential candidate due to their tuneable bandgap and balanced electron and hole diffusion lengths. Ti is a non-toxic and earth-abundant element with a stable oxidation state of +4 and excellent structural and optical properties [16]. The theoretical and experimental study of the optoelectronic properties of Cs_2TiX_6 (X = Cl, Br, I) suggests that these materials have potential applications in perovskite solar cells [32][33][34][35][36]. Ju et al. successfully synthesized a range of Ti-based VODHP in 2018, $Cs_2TiBr_{6-x}I_x$, using a melt crystallization method, followed by theoretical investigations [32]. Their results demonstrated that these Ti-based VODHPs possess desirable attributes, such as suitable band gaps, excellent optical absorption, and high stability, making them promising candidates for both single-junction and tandem photovoltaic applications. The bandgap of Ti-based VODHPs, can be tuned by

adjusting their stoichiometry, the type of halide used, and the synthesis process and parameters. As a result, these materials can exhibit a wide range of bandgaps, typically ranging from 0.9 eV to 1.8 eV, which makes them suitable for various optoelectronic applications, including but not limited to perovskite solar cells [32]. Additionally, they fabricated Cs_2TiBr_6 on TiO_2/FTO substrates via a two-step vapor deposition method, producing films with an acceptable band gap of 1.8 eV, extended carrier diffusion lengths exceeding 100 nm, appropriate energy levels, and robust environmental stability. The Cs_2TiBr_6 thin films achieved a PCE of approximately 3.3% [33]. Furthermore, Kong et al. demonstrated that Ti-based VODHPs, $Cs_2Ti(Br_xCl_{1-x})_6$, can be synthesized rapidly using an aqueous solution-based process at room temperature. The resulting materials exhibited tunable band gaps, strong optical absorption in the visible range, and excellent thermal stability [36]. These findings position the low-cost, solution-processed, Pb-free Cs_2TiX_6 VODHPs as promising candidates for next-generation eco-friendly optoelectronic devices.

Among other Ti-based VODHPs, Cesium titanium iodide (Cs_2TiI_6) has garnered significant attention because of its advantageous properties, such as a suitable bandgap for solar absorption and high stability [32]. Various methods have been employed to produce Cs_2TiI_6 VODHPs successfully, all in vacuum or inert atmospheres. The theoretical studies show that these VODHPs are highly stable and possess excellent optoelectronic properties [34]. It is observed that Cs_2TiI_6 VODHPs demonstrate high efficiency when applied as absorber materials in perovskite solar cells [37][38][39][40][41]. Table 1.1 shows various Ti-based VODHPs synthesized via multiple synthesis methods with their reported direct and indirect bandgaps.

Table 1.1: Ti-based VODHPs with different synthesis methods and reported bandgaps.

Ti- based VODHPs	Synthesis method	Experimental Bandgap (eV)	Atmosphere	Publication Year	References
Cs_2TiBr_6	Mechanochemical Ball milling	1.99 (direct) 1.88 (indirect)	Nitrogen	2023	[42]
Cs_2TiI_6		1.10 (direct) 1.02 (indirect)			
Cs_2TiBr_6	Melt crystallization	1.78 (direct)	Vacuum	2018	[32]
Cs_2TiI_6		1.02 (direct)			
Cs_2TiBr_6	Hot injection	2.3 (direct)	Argon	2021	[43]
Cs_2TiI_6		1.2 (direct)			
Cs_2TiBr_6	Hot injection	1.9 (indirect)	Nitrogen	2021	[44]
Cs_2TiCl_6		3.4 (indirect)			
Cs_2TiBr_6	Vapor deposition	1.82 (direct)	Nitrogen	2018	[33]
Cs_2TiCl_6	Solution-based	2.75 (direct) 2.54 (indirect)	Ambient conditions	2020	[36]
Cs_2TiBr_6		1.94 direct) 1.70 (indirect)			
Cs_2TiBr_6	Solution-based	2.0 (direct) 1.90 (indirect),	Nitrogen	2020	[45]
Cs_2TiBr_6	Solution-based	1.82 (direct)	Ambient Air	2023	[46]
Cs_2TiBr_6	Microwave-Mediated Synthesis	1.83 (indirect)	Nitrogen	2024	[47]

Overall, Cs_2TiI_6 VODHPs mark a significant step toward the development of environmentally friendly and high-performance photovoltaic technologies. This research focuses on the comprehensive exploration of Cs_2TiI_6 VODHPs by synthesizing them in ambient environment. By employing a solution-based synthesis approach, the study systematically investigates the structural, optical, and electrical properties of Cs_2TiI_6 VODHPs. The study also addresses various parameters such as precursor concentrations, solvents, and doping effects to achieve the optimal perovskite solution. The optimization of film formation is explored through different deposition techniques and annealing conditions to fully understand the intrinsic properties of Cs_2TiI_6

VODHPs. The current study describes the potential of Cs_2TiI_6 VODHPs as viable and promising absorbers to be used in solar cells. The ongoing research efforts are expected to drive the broader adoption of sustainable and efficient solar energy solutions, ultimately contributing to the global shift towards clean, renewable energy sources.

1.2 Originality of the Research

The originality of this research can be summarized through the following points:

- **i.** The synthesis of Cs_2TiI_6 VODHPs using a solution-based method has not been reported yet.
- **ii.** The effect of doping SnI_4 in Cs_2TiI_6 VODHPs has not been explored.
- **iii.** The fabrication of solar cells with Cs_2TiI_6 VODHP as an absorbing material has not yet been reported.

1.3 Problem Statement

Lead (Pb) halide-based perovskite materials have garnered significant interest in photovoltaics (PV) due to their remarkable improvement in PCE [48]. The exceptional performance of PSCs using Pb halide absorbers is attributed to their superior properties, including high carrier mobility, strong light absorption, and long electron-hole diffusion lengths. However, the toxicity of Pb halide-based PSCs poses a significant barrier to their commercialization. Pb exposure is harmful to human health, potentially causing muscle weakness, fatigue, and clumsiness. This has driven extensive efforts to develop stable and non-toxic perovskite materials for solar cells and other optoelectronic applications. Titanium (Ti)-based VODHPs are emerging as promising alternatives due to their tunable band gaps and inherently non-toxic nature. Ti is an

environmentally friendly element with a stable +4 oxidation state, providing an attractive alternative to Pb-based materials.

Ti-based vacancy-ordered double halide perovskites (VODHPs) have emerged as promising alternatives due to their inherently non-toxic nature, environmental stability, and tunable optoelectronic properties. Compared to other potential Pb-free candidates such as Sn, Ge, Bi, Pd, Te, and Zr-based perovskites, Ti offers distinct advantages. Unlike Sn-based perovskites, which suffer from oxidation instability ($Sn^{2+} \rightarrow Sn^{4+}$), Ti remains stable due to its fixed +4 oxidation state, reducing concerns of degradation. Similarly, Bi-based perovskites tend to have indirect bandgaps and lower charge carrier mobilities, which can limit their photovoltaic efficiency. The potential of Pd, Te, and Zr-based perovskites in photovoltaic applications has been explored; however, challenges such as stability, bandgap alignment, and fabrication feasibility remain limiting factors. Ti, on the other hand, provides an optimal balance between stability, bandgap tunability, and efficient charge transport, making it a highly attractive alternative for next-generation PV materials.

Among the Ti-based VODHPs, Cs_2TiI_6 stands out due to its potential advantages in optoelectronic applications. While Cs_2TiBr_6 and Cs_2TiCl_6 have been studied and show promise, Cs_2TiI_6 VODHP is particularly compelling due to its broader bandgap tuning range and potentially superior optical absorption properties. Cs_2TiI_6 VODHPs has a narrower bandgap (~1.2 eV) compared to Cs_2TiBr_6 VODHPs (~1.8 eV) and Cs_2TiCl_6 VODHPs (~2.3 eV). The larger ionic radius of iodine in Cs_2TiI_6 VODHPs contributes to its ability to absorb longer wavelengths of light, enhancing its optical absorption and making it more effective at utilizing a broader portion of the solar spectrum. This characteristic not only improves light harvesting but also increases the efficiency of photovoltaic devices. The combination of a narrower bandgap and superior

absorption capabilities makes Cs_2TiI_6 VODHPs a promising candidate for achieving higher PCEs in solar cells and other optoelectronic applications.

To date, there is limited information on the synthesis of Cs_2TiI_6 VODHPs, and the mechanisms underlying film formation are not fully understood. Existing synthesis methods, such as hot-injection, melt crystallization, and mechano-chemical ball milling methods, are complex and require high temperatures [32][42] [43]. Notably, no research has reported the synthesis of Cs_2TiI_6 VODHPs using a solution-based approach. Cs_2TiBr_6 VODHPs synthesized via solution-based methods has shown instability, leading to poor air stability and decomposition into CsBr upon exposure to oxygen [36][45].

This study aims to address this gap by exploring solution-based synthesis methods for Cs_2TiI_6 VODHPs to improve its practical applicability and performance. The research will comprehensively characterize the crystal structure, crystallinity, and surface morphology of Cs_2TiI_6 VODHP films to understand the material's fundamental properties. Additionally, it will investigate the mechanisms of film formation under various synthesis parameters to optimize the process and enhance the material's quality. The research also includes an in-depth analysis of the optoelectronic properties of Cs_2TiI_6 VODHPs films, such as optical absorption, carrier mobility, and stability. Finally, the performance of solar cells utilizing Cs_2TiI_6 VODHPs as the absorber layer will be evaluated, examining charge transport mechanisms, efficiency metrics, and overall device performance to assess its potential for high-efficiency photovoltaic applications and establish Cs_2TiI_6 VODHPs as a viable alternative for next-generation solar technologies.

1.4 Objectives

i. To optimize the synthesis parameters and identify the crystal structure, composition, and surface morphology of Cs_2TiI_6 VODHPs films synthesized via a simple solution-based process.

ii. To propose the film formation mechanism, optical properties, and electrical properties of Cs_2TiI_6 VODHPs films.

iii. To evaluate the viability of Cs_2TiI_6 VODHPs as a solar cell absorber and assess its potential for application in photovoltaic devices.

1.5 Scope of Research

The scope of this research encompasses a comprehensive exploration and development of Cs_2TiI_6 perovskite films for solar cell applications. It begins with the synthesis and optimization of the solution-based synthesis method, by varying the precursor concentrations, types of solvents, and synthesis temperatures. Furthermore, the research will investigate the effect of SnI_4 doping on the structural, optical, and electrical properties of Cs_2TiI_6 VODHPs, evaluating the potential improvements in material performance due to doping.

Additionally, the research will investigate the mechanisms underlying the formation of Cs_2TiI_6 films and analyze the impact of synthesis parameters on film quality and uniformity. Various analytical techniques will be employed to characterize the crystal structure, composition, and surface morphology of the synthesized films. The study will also explore the optical and electrical properties of Cs_2TiI_6 VODHP films, including absorption spectra, bandgap determination, conductivity, and carrier mobility. This analysis will help to understand the material's potential in photovoltaic applications.

In terms of practical application, the research will focus on fabricating and testing solar cells using Cs_2TiI_6 VODHP as the absorber layer. This involves optimizing the device architecture and fabrication processes to achieve high-efficiency solar cells. A comparative analysis will also be conducted to evaluate the performance of Cs_2TiI_6-based solar cells against conventional perovskite materials, identifying the advantages and limitations of Cs_2TiI_6 VODHPs in photovoltaic applications. By addressing these areas, the research aims to provide a detailed understanding of Cs_2TiI_6 VODHP's properties and their potential as a viable alternative to Pb-based perovskite in solar cell technology. This study will contribute to the advancement of environmentally friendly and efficient photovoltaic materials.

1.6 Research Questions

i. What is the crystal structure, composition, and surface morphology of Cs_2TiI_6 films synthesized via the solution-based method?

ii. What impact do different synthesis parameters have on the film formation optical and electrical properties of Cs_2TiI_6 perovskite?

iii. What is the potential of Cs_2TiI_6 as an absorber material in perovskite solar cells, and how does this material contribute to the performance of solar cells?

1.7 Thesis Outline

This thesis is comprised of five chapters.

In **Chapter 1**, the general overview of VODHPs has been discussed. The chapter discusses the need to explore alternative materials to replace Pb due to the toxicity and inadequate stability of the current perovskite solar cell technology. The research

problem statement, research objectives, and scope and originality of research are presented.

Chapter 2 provides literature review, theoretical background, and perovskite advancements. This chapter specifically focuses on Pb-free perovskites, offering a contextual framework for understanding the latest developments in perovskite research. Additionally, it details the synthesis methods employed for Ti-based VODHPs, covering their crystal structures, optical properties, and stability. The chapter concludes with the recent studies on Ti-based VODHPs in solar cell applications.

In **Chapter 3**, the focus is on detailing the methodologies and instrumentation employed for characterizing perovskite materials. This chapter comprehensively examines the techniques and tools utilized in the research process to analyze and understand the structural, optical, and electric properties of perovskite materials.

The results and discussion are presented in **Chapter 4**. This chapter presents and analyzes the results obtained through the synthesis process, shedding light on the structural, morphological, and potentially optoelectronic characteristics of the Cs_2TiI_6 perovskite materials. Moreover, the practical viability of Cs_2TiI_6 perovskite as a component in solar cell devices is also discussed.

Finally, **Chapter 5** concludes and summarizes the contents of previous chapters and outlines the necessary future work required to enhance the performance of perovskite solar cells. Additionally, recommendations for potential extensions of this study are suggested.

CHAPTER 2

LITERATURE REVIEW

2.1 Introduction

The literature review in this chapter extensively explores perovskite solar cells, covering their fundamental aspects and recent advancements. It begins by discussing the evolution of perovskites from oxides to halides, followed by an exploration of their semiconducting properties and crystal structures. The chapter then reviews various families of perovskites, including single halides, double halides, and VODHPs, highlighting the transition from Pb-based to Pb-free materials. The comparative analysis highlights their distinct properties, advantages, and challenges, offering insights into the diverse materials used in perovskite solar cell fabrication. The potential of Ti-based VODHPs as a promising research avenue is emphasized, with an in-depth look at their synthesis methods and relevant properties. The chapter concludes with a detailed examination of perovskite solar cells, including their history, working principles, device architecture, and materials, with a specific focus on the challenges and recent studies related to Ti-based VODHPs in solar cell applications.

2.2 Perovskites

The name ***"Perovskite"*** originated after the name of a Russian mineralogist, L.A. Perovski, who discovered the first perovskite, calcium titanium oxide ($CaTiO_3$), in 1839 [49]. Later, many inorganic metal oxides, such as $BaTiO_3$, $PbTiO_3$, $SrTiO_3$, $BiFeO_3$, etc., were found to have similar perovskite structure, with formula ABO_3. These oxide perovskites found applications in ferroelectric, piezoelectric, dielectric, and pyroelectric fields but were not suitable for photovoltaic (PV) applications due to inadequate

semiconducting properties, except for a few compositions like $LiNbO_3$, $PbTiO_3$, and $BiFeO_3$ [50].

Conversely, halide perovskites exhibit desirable semiconducting properties for PV applications, where halide anions replace oxide anions (ABX_3; A = cation (MA, FA,Cs^+), B = divalent metal cation (Pb, Sn, Ge, Ti), X = halogen anions (I^-, Br^-, Cl^-)). Halide perovskites were first explored in the 1890s by Wells et al., who synthesized Pb halide compounds like $CsPbX_3$ (X = Cl, Br, I) [51]. The simple solution synthesis of cesium lead halide ionic crystals led to the exploration of other cations, such as methylammonium ($CH_3NH_3^+$), resulting in organic lead halide perovskites [52]. By the late 20th century, a broad range of halide perovskites were synthesized using various organic cations [53][54][55].

Today, the range of halide perovskites includes materials with diverse band gap energies, from $MASnI_3$ (1.1 eV) to $MAPbI_3$ (1.6 eV), $MAPbBr_3$ (2.3 eV), and $MAPbCl_3$ (3.1 eV) [56]. The ability to fine-tune the cation (MA+, Cs+, FA+, Rb+, etc.) and anion (Cl-, Br-, I-, etc.) compositions allows for a wide absorption spectrum, making these materials suitable not only for PV applications but also for various optoelectronic devices like LEDs [57], photodetectors [58], lasers [59]. The following properties make them well-suited for photovoltaic (PV) applications. Here are the good properties of halides over oxides:

(a) High Absorption coefficient

Halide perovskites, such as $MAPbI_3$, demonstrate outstanding PV performance due to their exceptional absorption coefficients, up to 10^5 $cm^{-1,}$ from UV to visible light [60]. This is significantly higher than traditional materials like GaAs, allowing for ultra-thin absorber layers (~500 nm) [61]. The band gap of perovskites ranges from 1.4 to 3.0

eV, covering the entire visible spectrum, making them versatile for various applications [62][63].

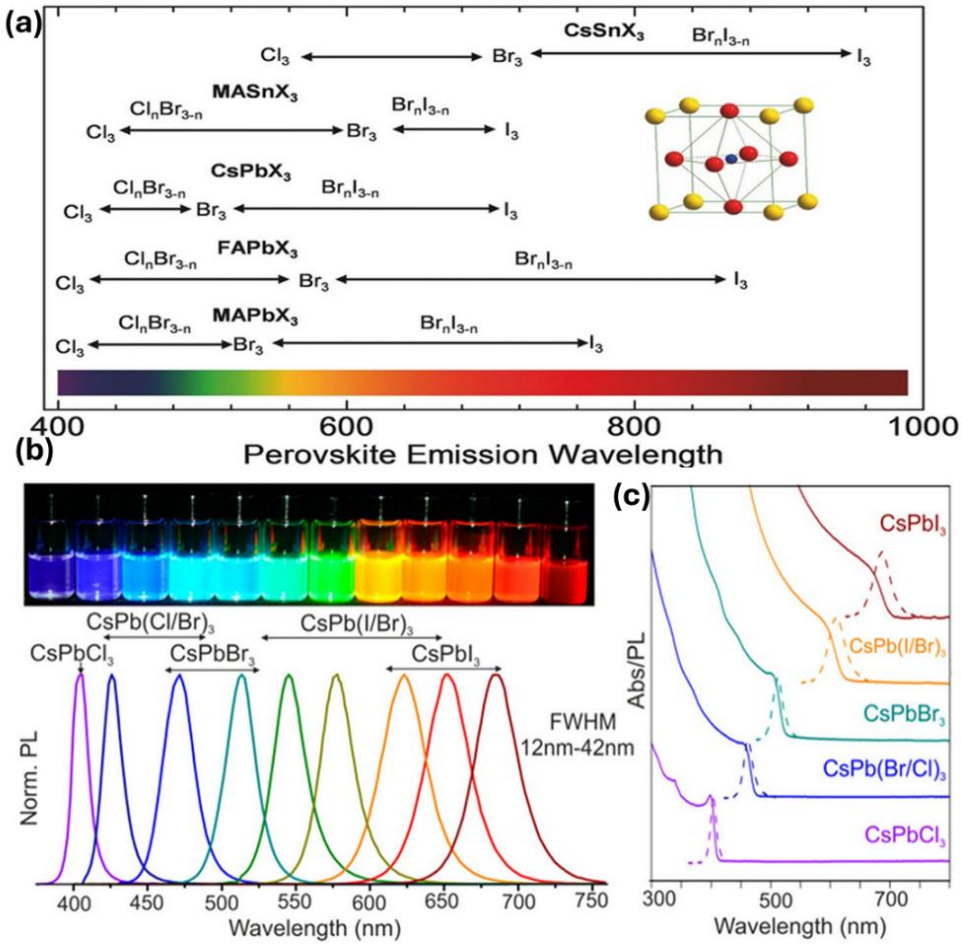

Figure 2.1: (a) Perovskite emission wavelength tuning by halide composition, (b) Photoluminescence spectra of $CsPbX_3$ perovskites with varying halide ratios, (c) Absorption and PL spectra of $CsPbX_3$ perovskites showing bandgap tunability [63][64].

Figures 2.1 (a) and (b) illustrate the absorption and emission spectra of perovskites: organic $MAPbX_3$ covers 390–790 nm, while inorganic $CsPbX_3$ covers 400–710 nm. The tunable absorption and fluorescence spectra, through composition adjustments, enhance their adaptability (2.1 (c)). A notably low urbach energy of 15 meV in $MAPbI_3$ highlights its purity and absence of deep trap states, contributing to V_{OC} and FF in solar cells [65].

(b) Long carrier diffusion length:

Perovskites exhibit exceptional carrier diffusion lengths and mobilities, making them ideal for high-performance devices. In $MAPbI_3$ single crystals, carrier diffusion lengths reach approximately 175 μm [66]. Hole mobilities exceed 100 $cm^2/V{\cdot}s$, and electron mobilities are around 24 $cm^2/V{\cdot}s$, as measured by space-charge-limited current (SCLC), Hall effect, and time-of-flight techniques. The consistency among these measurements indicates minimal band-tail states [67]. Perovskites like $MAPbI_3$ also demonstrate higher ion conductivity than electronic conductivity, emphasizing the role of ion transport. Various characterization methods have identified I^- ions as the primary conductive species in $MAPbI_3$, indicating that ion conductance is mainly facilitated by halogen ions [68][69]. Light conditions significantly enhance both electronic and ion conductance, with ion conductance increasing by three orders of magnitude due to the elevated chemical potential of I^- ions promoting migration [70]. Hence, the success of planar structure perovskite solar cells is attributed to their excellent light absorption capabilities, capturing sunlight up to 800 nm, and their remarkable electron and hole transportation properties.

(c) Unique defects physics:

In PV applications, the defect-tolerant nature of halide perovskites holds significant importance, particularly in achieving high-voltage output. The high PCE of PSCs results from their high photovoltage output, typically ranging from 1.1 to 1.2 V [71], rather than high photocurrent. Unlike silicon solar cells, which suffer from voltage losses due to impurity defects and thermal effects, PSCs maintain voltage stability even under low light. High-efficiency PSCs often exceed V_{OC} of 1.1 V, with some achieving over 1.2 V, relative to their band gap energy of 1.55–1.6 eV [72].

Despite this, PSCs still experience V_{OC} losses, primarily due to defect (trap) densities, ranging from 10^{10} cm^{-3} (single crystals) [67][73] to 10^{16} cm^{-3} (polycrystals) [74][75]. However, shallow defect traps in halide perovskites can be easily detrapped, allowing them to contribute to the current generation, thus minimizing the adverse impact on photovoltaic performance.

2.3 Structure of Perovskites

Perovskites follow the ABX_3 formula, with 'A' and 'B' as cations and 'X' as an anion, typically oxygen or a halide. In PV solar cells, halide perovskites are used rather than oxide perovskites. Halide perovskites are further categorized into alkali-halide and organic-inorganic types, with methylammonium lead iodide ($MAPbI_3$) being a typical example [76][77][78]. The basic structure of perovskite is cubic, with 'A' at the centre and BX_6 octahedra sharing corners. Figure 2.2 illustrates the most common elements or compounds used for the A, B, and X sites in perovskite.

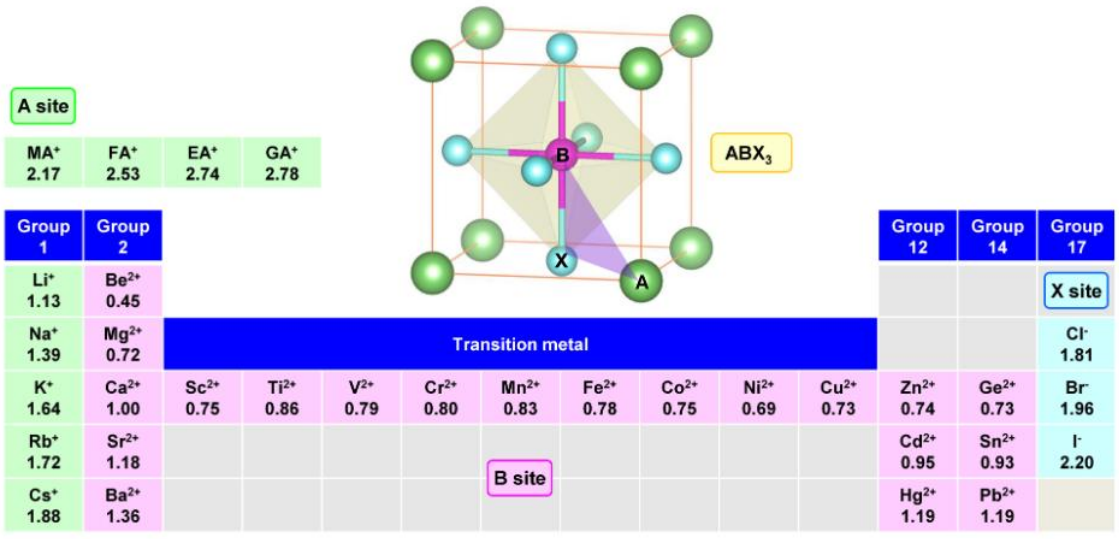

Figure 2.2: Crystal structure of ABX_3 perovskite and commonly used elements at A, B, and X sites, along with their ionic radii (in Å) [79].

Depending on what those components are and their relative sizes to each other, it is possible to stress the crystal out of its normal shape into several other alternate perovskite structures. Stressing a crystal by altering a crystal's components is a well-accepted method of modifying both physical and electronic properties [80][81][82].

Changing the halide component (X) can rotate the octahedral structures, shifting the lattice from cubic to tetragonal or orthorhombic forms [83]. External stimuli such as temperature and pressure can also induce structural changes [84]. Substituting part of the B component creates double perovskites, allowing for modifications like removing Pb or inducing ferroelectric effects [85]. Adjusting the B and X elements customizes the band gap, with $CH_3NH_3PbX_3$ (X = Cl, Br, I) showing a band gap increase from 1.5 to 2.3 eV as halides change from iodide to chloride. This is because the X ion's electronegativity and ionic radius decrease.

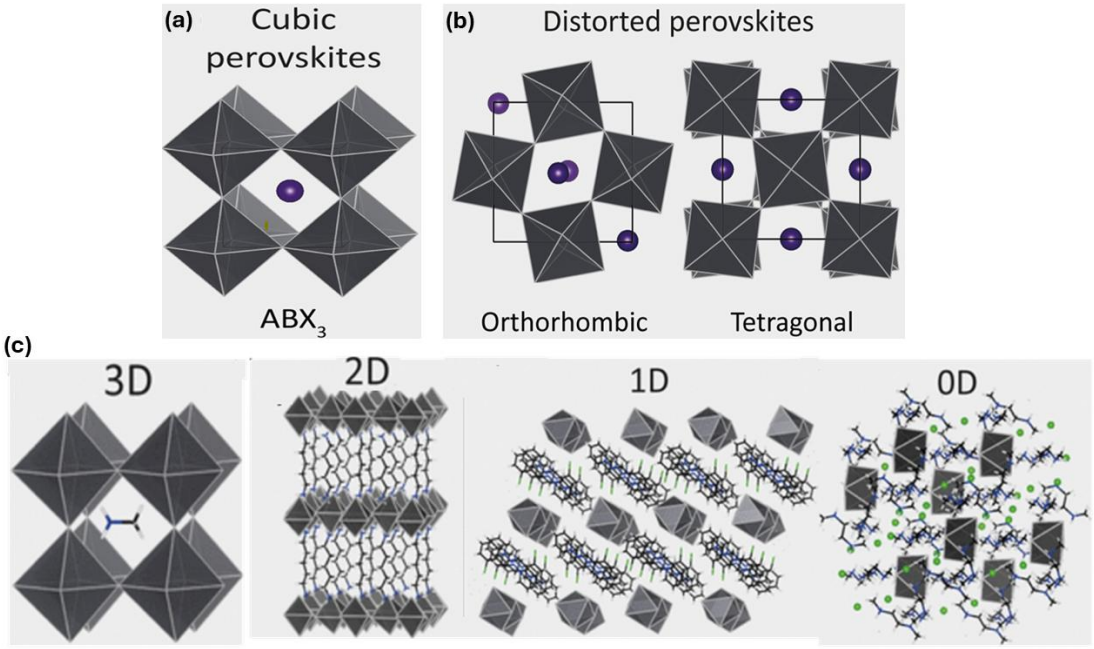

Figure 2.3: Overview of halide perovskites (a) Standard ABX_3 cubic halide perovskites, (b) Common orthorhombic and tetragonal disordered perovskites arise from the octahedra tilting [86] and (c) 3D, 2D, 1D, and 0D crystal structures of ABX_3 perovskites.

The A component's size can shift the structure from 3D ABX_3 to 2D forms like A_2BX_4 or $A_3B_2X_7$ [84][86]. The B and X ions primarily influence the electronic properties, which determine the conduction and valence bands. Two important empirical parameters assess the degree of distortion and stability of perovskites, the Goldschmidt tolerance factor (t) and the octahedral factor (μ), which are defined as follows:

$$t = \frac{r_A + r_X}{\sqrt{2}(r_B + r_X)} \quad 2.1$$

$$\mu = \frac{r_B}{r_X} \quad 2.2$$

where r_A, r_B, and r_X are the ionic radii of A, B, and X, respectively. The octahedral factor measures the degree of distortion of the octahedron, whereas the tolerance factor gauges the degree of fit between the A cation and the BX_6 octahedron. In addition, $t = 1$ and $\mu = 1$ represent the ideal perovskite structure, while deviating from these values signifies instability and distortion in the structure. VODHP structures are generally stable at $0.8 < t < 1.00$ and $0.29 < \mu < 0.55$ [87]. While the cubic perovskite's ideal t value is 1, most perovskites have lower symmetries, such as tetragonal, orthorhombic, rhombohedral, or mono-clinic, and deviate from this ideal structure [88].

2.4 Family of perovskites

2.4.1 Single halide perovskites

Halide perovskites, represented by the formula ABX_3, are extensively researched for their photovoltaic applications. Common A-site cations include MA, FA, and Cs, influencing the optoelectronic properties through the $[BX_6]^{4-}$, octahedral framework [89]. Notably, $MAPbI_3$ and $FAPbI_3$ are widely studied examples with

optical bandgaps of ~1.55 eV and ~1.48 eV, respectively [90][91]. The larger bandgap of $MAPbI_3$ restricts its PCE, compounded by poor thermal stability due to the escape of methylammonium ions (MA^+) at high temperatures (above 85 °C) [92]. Substituting MA with FA leads to a cubic assembly with a slightly larger lattice and reduces the bandgap to 1.45–1.52 eV in $FAPbI_3$, enhancing light absorption [93][94].

Recent studies have shown that modifying the composition, such as adding 25% MAI or doping with Cs, can significantly improve device performance, demonstrating efficiencies up to 14.98% [95][96]. It is well known that Pb is toxic and not environment-friendly, so seeking Pb-free perovskites with high efficiency is an urgent task. A typical example of a non-toxic inorganic halide perovskite is $CsSnI_3$; based on this, the efficiency of solution-processed solar cells has remained at a moderate range of 5 %–6.5 %. The perovskite $CsSnI_3$ is moisture-sensitive and unstable in the air [97]. Recently, $CsSnI_3$ perovskite has achieved an efficiency of over 12% by surface post-treatment with bi-functional polar molecules [98].

2.4.2 Double halide perovskites

Recently, interest in halide double perovskites (HDPs) has grown significantly. HDPs, denoted by the formula $A_2B^+B^{3+}X_6$, are formed by replacing two Pb^{2+} ions with one monovalent cation B^+ and one trivalent B^{3+} ion. Structurally, these double perovskites exhibit a similar 3D arrangement as Pb perovskites, featuring alternating octahedral formations of $[B^+X_6]^{5-}$ and $[B^{3+}X_6]^{3-}$ with A-site cations occupying the cavities created by these octahedra (Figure 2.4 (a) and (b)).

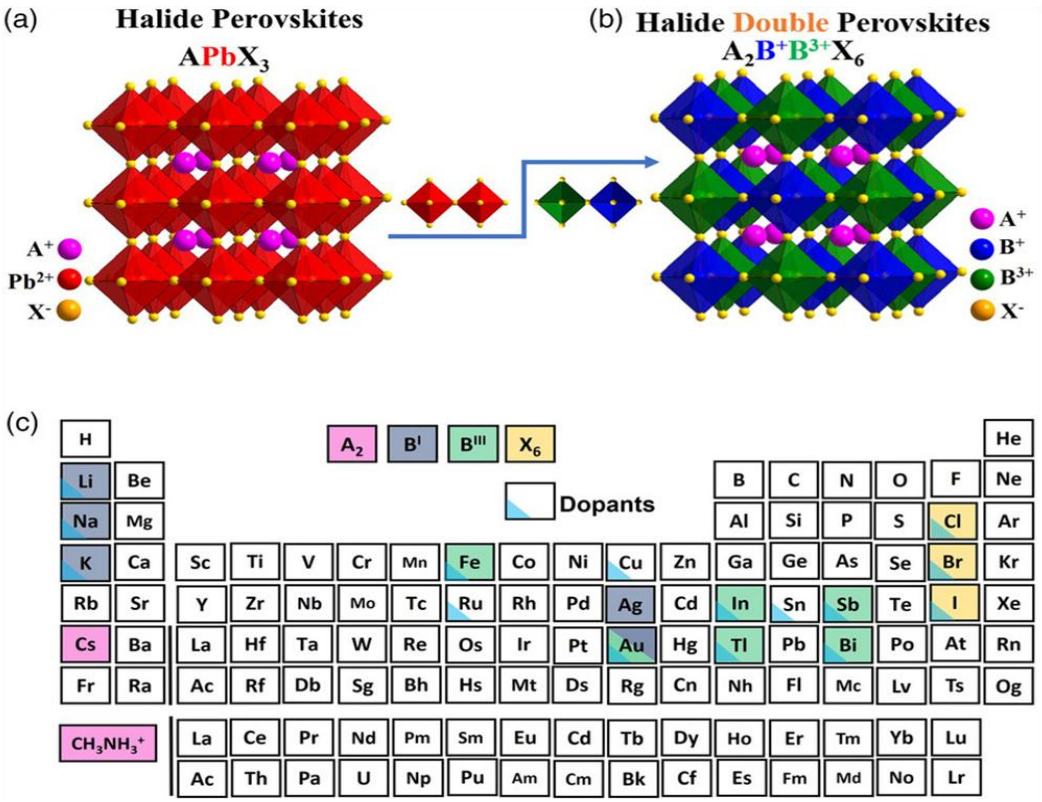

Figure 2.4: (a) and (b) Schematic view of B^+/B^{3+} cation substitution from Pb halide perovskites ($APbX_3$) to double perovskites ($A_2B^+B^{3+}X_6$) [99], (c) Selection of cations and anions for $A_2B^+B^{3+}X_6$ perovskites.

The selection of A cation and X anion is relatively limited, with Cs^+ and $CH_3NH_3^+$ (MA^+) being the primary choices for A cations, while Cl^-, Br^-, and I^- are the dominant X anions (Figure 2.4 (c)). On the other hand, the options for B-site cations are more varied and include Ag^+, Na^+, Li^+, Au^+, Bi^{3+}, Sb^{3+}, In^{3+}, Fe^{3+}, Tl^{3+} etc. [100]. Despite their potential, these halides exhibit high ionicity and large bandgaps (>1.9 eV), limiting their suitability for single junction PV applications [101]. Over the past years, various HDPs have been synthesized, such as Cs_2AgBiX_6 (X = Br, Cl) [102][103], $(MA)_2KBiCl_6$ [104], $Cs_2AgInCl_6$ [105] $Cs_2AgSbCl_6$ [106] and $(MA)_2TlBiBr_6$ [107]. Among these, $Cs_2AgBiBr_6$ stands out with the smallest bandgap of 1.95 eV, which holds potential for use in tandem and multijunction PVs [102]. Figure 2.5 (c), (d) and (e) shows that its optical bandgap varies between 1.95–2.19 eV [85][108][109], with PL showcasing peaks at 1.87 eV (room temperature and a relatively narrow peak at 1.98 eV

(22.6 K) [102]. Time-resolved PL (Figure 2.5 (f)) reveals rapid initial decay followed by slower behaviour in powders and single crystals. Additionally, $Cs_2AgBiBr_6$ demonstrates excellent moisture, light, and thermal stability [102].

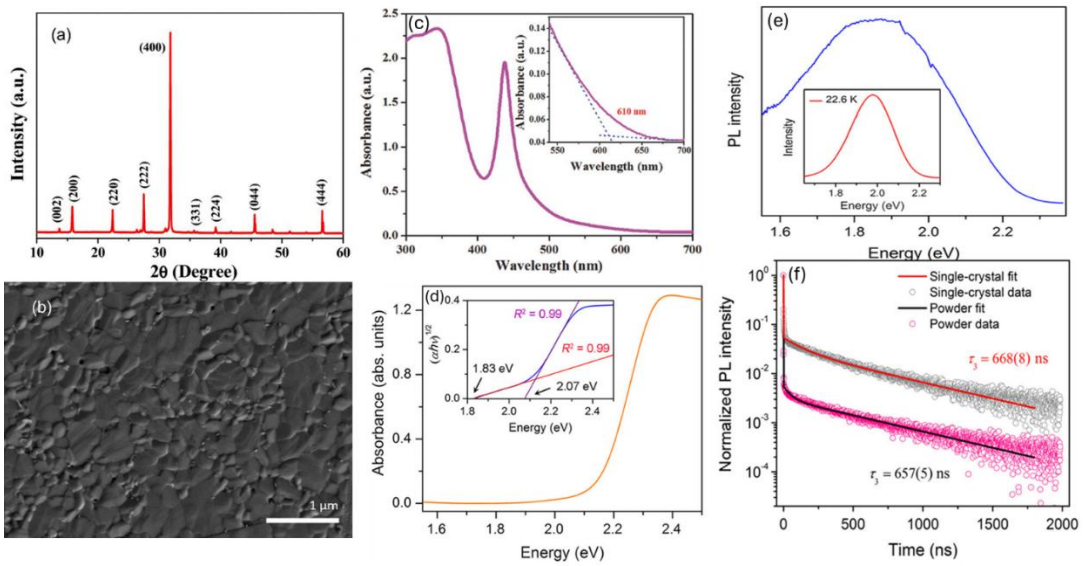

Figure 2.5: (a) XRD pattern and (b) SEM image of the prepared $Cs_2AgBiBr_6$ double perovskite thin films [110] (c) Typical absorption spectrum of $Cs_2AgBiBr_6$ films with the inset showing the absorption onset at 610 nm [109] (d) Absorbance spectrum of $Cs_2AgBiBr_6$ powder (Inset: Tauc plot showing the characteristics of an indirect bandgap) [102] (e) Steady-state room-temperature PL spectrum of a powdered $Cs_2AgBiBr_6$ sample upon 500 nm excitation. (Inset: low-temperature PL spectrum) [102] (f) Time-resolved room-temperature PL and fits for the PL decay time (τ) in powder and single-crystal samples) [102].

While I-based double perovskites present smaller bandgaps than their Br^- and Cl^- based counterparts, the successful synthesis of I^- based double perovskites remains challenging due to thermodynamic instability [111]. In-based and Cu-based double perovskites such as $Cs_2InBiCl_6$, $Cs_2InBiCl_6$, and Cu(I)-based $Cs_2CuInBr_6$ are also considered promising PV absorber candidate materials, with suitable bandgaps suitable for single-junctions [112][113]. However, there have been no reports of their successful synthesis due to their thermal instability.

Table 2.1: Summary of various HDPs synthesized by various techniques.

Stoichiometry	Perovskite	Synthesis Route	Bandgap		References
			Exp. (eV)	Theoretical (eV)	
2-1-1-6	$Cs_2AgInCl_6$	Solvent evaporation	3.3 (direct)	2.7	[105]
		Hydrothermal	3.23 (direct)	3.33	[114]
	$Cs_2AgBiCl_6$	Solvent evaporation	2.77 (indirect)	2.62	[108]
		Solid state	2.2 (indirect)	2.4	[85]
		Solid state/solvent evaporation	2.4 (indirect)	-	[115]
	$Cs_2AgBiBr_6$	Solvent evaporation	2.19 (indirect)	2.06	[108]
		Solid state	1.9 (indirect)	1.8	[115]
		Solid cooling	1.95 (indirect)	-	[102]
		Hydrothermal	2.05 (direct)	-	[109]
	Cs_2AgBiI_6	-	-	1.6	[85]
	$Cs_2AuBiCl_6$	-	-	1.6	[85]
	$Cs_2AuBiBr_6$	-	-	1.1	[85]
	Cs_2AuBiI_6	-	-	0.5	[85]
	$Cs_2CuBiCl_6$	-	-	2.0	[85]
	$Cs_2CuBiBr_6$	-	-	1.9	[85]
	Cs_2CuBiI_6	-	-	1.3	[85]
	$Cs_2AgInBr_6$	-	-	1.50	[112]
	$Rb_2AgInCl_6$	-	-	2.5	[112]
	$Rb_2AgInBr_6$	-	-	1.46	[112]
	$Rb_2CuInCl_6$	-	-	1.36	[112]
	$Rb_2CuInBr_6$	-	-	0.63	[112]
	$(MA)_2AgBiBr_6$	Hydrothermal	2.0 (indirect)	2.02	[116]
	$(MA)_2KBiCl_6$	Hydrothermal	3.04 (indirect)	3.08	[117]
	$(MA)_2AgSbI_6$	Solid state	1.93 (indirect)	2.12	[118]
2-1-6	Cs_2SnI_6	Solution-processed	1.25 (direct)	0.97	[26]
	Cs_2SnI_6	Evaporation	1.48 (direct)	-	[27]
	Cs_2TiI_6	Melt-crystallization	1.02 (direct)	1.05	[32]
	Cs_2TiBr_6	Melt-crystallization	1.78 (direct)	1.89	[32]
	Cs_2TiBr_6	Vapour based	1.8 (direct)	-	[33]
	Cs_2TeI_6	Solution method	1.50 (indirect)	-	[30]
	Cs_2TeI_6	Solution-processed	1.59 (indirect)	1.83	[26]
	Cs_2PtI_6	solvent replacement method	1.37 (indirect)	-	[119]
	Cs_2PdI_6	antisolvent method	1.49 (direct)	-	[120]

	Cs_2PdBr_6	antisolvent method	1.69 (direct)	-	[120]
	Rb_2SnI_6	solution precipitation	1.32 (direct)	1.13	[121]
	MA_2SnI_6	thermal evaporation	1.81(direct)	-	[122]
3-2-9	$Cs_3Sb_2I_9$	Solution-processed	2.2 (direct)	-	[123]
	$MA_3Sb_2I_9$	solvent engineering techniques	2.14 (direct)	-	[124]
	$Rb_3Sb_2I_9$	Solution-processed	2.24 (direct)	-	[125]

2.4.3 Vacancy ordered double halide perovskites

Vacancy-ordered double halide perovskites (VODHPs) are a subclass of double perovskite materials characterized by precise vacancies within their crystal structure, offering enhanced stability. These materials derive from doubling the ABX_3 perovskite unit cell along three axes and removing alternate B-site cations, resulting in an ordered face-centered cubic arrangement (Figure 2.6) [126].

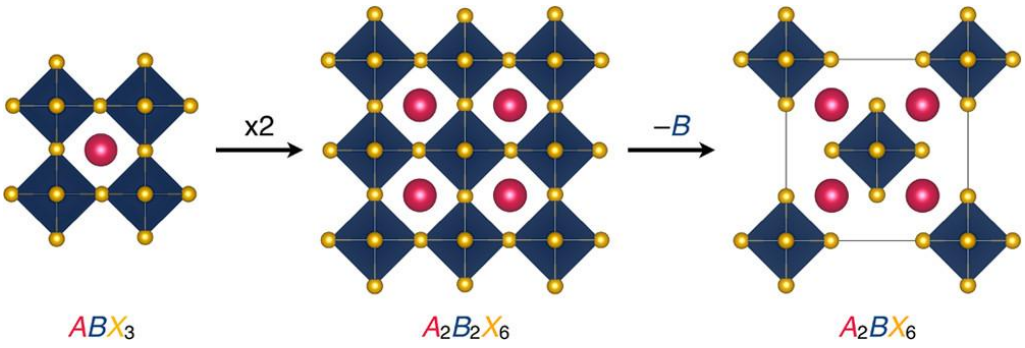

Figure 2.6: Schematic of the relationship between ABX_3 perovskite and A_2BX_6 (vacancy-ordered) double perovskite [17].

These compounds are also viewed as 0D perovskites since the $[BX_6]$ octahedra are not corner-sharing but are isolated [127]. Compared with the conventional ABX_3 structure, the VODHPs, A_2BX_6 structure has a tetravalent B-cation instead of a bivalent

B-cation in ABX_3, which endows it with enhanced air and moisture stability under ambient.

The most common example within this category is Cs_2SnI_6, which showcases a direct bandgap of approximately 1.3 eV, making it exceptionally suitable for single-junction PV systems [23]. Studies have demonstrated the ability to adjust the bandgap of Cs_2SnI_6 extensively, reaching up to 2.9 eV and 3.9 eV by substituting I^- with Br^- and Cl^- respectively [99][21]. The compound exhibits strong absorption, N-type conductivity, and moisture stability [23][25]. Due to the tetravalent character of Sn, Cs_2SnI_6 exhibits higher air stability than $CsSnI_3$ [128]. Cs_2PdBr_6 nanocrystals with an average diameter of 2.8 nm also displayed high stability against light illumination (one sun for more than 1000 h), moisture (70% for two months), and high temperature (120 °C for 600 h), with a narrow direct bandgap of 1.69 eV [120]. Research on Ti-based VODHPs, dating back to the early 1960s, gained traction in optoelectronics in 2018 with the introduction of $Cs_2TiI_xBr_{6-x}$ ($x = 0, 2, 4, 6$) powders demonstrating tunable bandgaps from 1.02 to 1.78 eV [32]. This novel synthesis method enabled the continuous tuning of bandgaps from 1.02 to 1.78 eV. These newly investigated VODHPs exhibit appealing characteristics such as remarkable stability, suitable direct bandgaps, exceptional optical absorption, and benign defect properties.

The concept of VODHP extends to novel compounds with the formula unit $A_3B_2X_9$, featuring a monovalent cation A and a trivalent metal cation B [129][124]. These compounds typically have band gaps around 2.1 eV and demonstrate improved air stability compared to $MAPbI_3$. They have been integrated into heterojunction solar cells, achieving PCEs suitable for various PV applications [123] [125].